Dirac degeneracy and elastic topological valley modes induced by local resonant states

Quan Zhang, Yi Chen, Kai Zhang,* and Gengkai Hu†
Key Laboratory of Dynamics and Control of Flight Vehicle, Ministry of Education, School of Aerospace Engineering, Beijing Institute of Technology, Beijing 100081, China

(Received 4 September 2019; published 7 January 2020)

In elastic systems, the current technique to produce Dirac degeneracy is based on Bragg scattering eigenstates, which, however, suffers from operating only at relatively high frequency determined by lattice constant. Here, an elastic metamaterial plate that presents an analog to the quantum valley Hall effect (QVHE) is proposed to achieve Dirac degeneracy with local resonant states, enabling us to tune the operating frequency without altering the lattice. By introducing resonator pair into a hexagonal lattice, a local resonance states-induced Dirac cone is produced right below the local resonant band gap caused by the resonator pair. After gapping the Dirac cone with unequal masses of the resonator pair, a new local resonant band gap supporting topological edge modes immune to backscattering appears. This band gap is formed by mixing effective negative mass effect and Bragg scattering effect due to large virtual mass. These ideas are demonstrated by numerical simulation, as well as validated by the experiment on flexural wave in a textured plate. The proposed design provides a new degree of freedom to control elastic topological mode and paves the way to explore subwavelength elastic topological interface states.

DOI: 10.1103/PhysRevB.101.014101

I. INTRODUCTION

The recent advent of topological phases has attracted researchers to explore novel topological states in condensed matter physics [1]. One of the most impressive features is that the domain wall between two materials with distinct topological indices supports edge waves immune to defects and sharp corners. Originally discovered in quantum physics, these topological phases are quickly extended to other classical fields such as photonics [2–4], acoustics [5–8], and mechanics [9,10].

In a solid-state elastic system, three commonly used ways have been achieved to realize topological protections. The early designs were based on the mimic of quantum Hall effect (QHE), which requires external field interacting with the wave medium to break time-reversal symmetry (TRS). The most commonly used method to break TRS was by exploiting spinning rotors [11,12]. The second and third ways only used passive components, which were developed by analogy with quantum spin Hall effect (QSHE) [13–18] and quantum valley Hall effect (QVHE) [19–23], respectively. Recently, a single platform supporting multiple classes of topological modes was also reported [24]. Generally, Dirac degeneracy plays a key role in these designs to achieve topological protections. It is shown that the material with C_{3v} lattice symmetry has deterministic Dirac-like degeneracies at the high-symmetry points in the Brillouin zone [15]. However, these Dirac degeneracies are constructed by the Bragg scattering eigenstates, and their frequencies are determined by the lattice constant. This means lowering the operating frequency generally demands large lattice size due to the Bragg condition. To circumvent this limitation, degenerated eigenstates independent of lattice constant are required.

By introducing resonators, the subwavelength topological edge states could be achieved for photonics [25] and airborne acoustics [26–29]. For a solid-state elastic system, Chaunsali *et al.* [30] reported subwavelength Dirac cone and corresponding edge states in a thin plate attached with resonators. The similar structure was also studied by Torrent *et al.* [31] and Pal *et al.* [32]. In these works, the stiffness of the resonator is comparable to that of the substrate, which results in Dirac eigenstates still dominated by Bragg scattering states. Chaunsali *et al.* [33] also proposed a design of bolted plate to realize topological flexural wave guiding, where the local resonance of the bolts was exploited to eliminate unwanted in-plane plate modes rather than to construct Dirac degeneracies. Wang *et al.* [34] presented a symmetric double-sided pillared phononic crystal which can emulate both QVHE and QSHE. In this study, the locally resonant mode of the pillar was exploited to enhance the edge state since it became evanescent in the deep subwavelength scale. Although resonators have been used in these designs, when the Dirac cone is lifted, the formed topological band gap still belongs to Bragg band gap instead of local resonant band gap. Whether topological edge states can emerge in local resonant band gap with effective negative mass density is still an open question.

In the present study, we propose an elastic metamaterial plate that presents an analog to the QVHE, enabling to achieve degenerated eigenstates independent of the lattice constant for elastic waves. A deterministic Dirac cone is demonstrated to form near the nature frequency of local resonators. After gapping the Dirac cone, both the numerical simulations and experiments demonstrate that elastic topological edge modes exist in the newly formed local resonant band gap with

*zhangkai@bit.edu.cn
†hugeng@bit.edu.cn

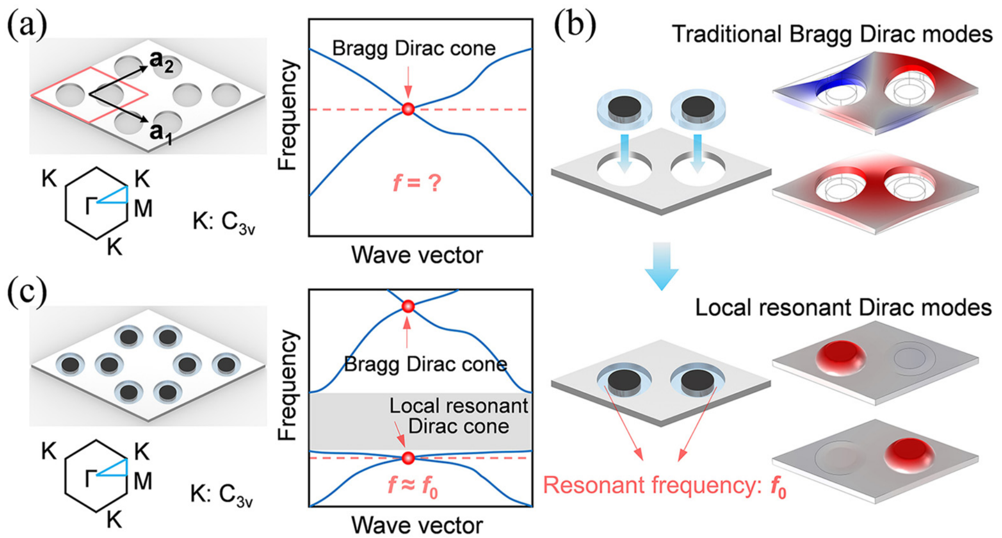

FIG. 1. The principle scheme of local resonance states induced Dirac degeneracy. (a) The traditional elastic valley Hall insulator. (b) A resonator pair is introduced into the classic valley Hall insulator. (c) The obtained local resonant valley Hall insulator.

singular effective mass density, which hasn't been reported by previous researches.

II. RESULTS

A. Demonstration of the existence of local resonant Dirac cone based on hexagonal spring-mass lattice

Considering a typical hexagonal lattice [Fig. 1(a)], a K-point Dirac cone at relatively high frequency determined by the lattice constant is observed since the Brillouin zone (BZ) corner points possess C_{3v} symmetry. To construct a new Dirac cone at lower frequency, a resonator pair is introduced into the system without changing the lattice constant [Fig. 1(b)]. Consequently, a new Dirac cone appears right below the local resonant band gap (BG); see Fig. 1(c). The local resonant Dirac mode is radically different from the traditional Bragg Dirac mode [Fig. 1(b)] and depends mainly on the introduced local resonator. Therefore, we can tune the position of the Dirac cone by adjusting local resonator without modifying the lattice constant.

We first demonstrate the existence of a deterministic Dirac cone and corresponding valley Hall edge state nearby the natural frequency of the resonators. The studied discrete hexagonal lattice is illustrated in Fig. 2(a). The representative unit is highlighted by a grey diamond, and the lattice constant L is assumed to be 1. Each unit cell has two sites respectively denoted as p and q with equal mass M. Besides, there is a local resonator inside of each site block, and the resonators in p and q are represented by r and s respectively. The masses of the resonator r and s are denoted by m_r and m_s, respectively. Here we only consider the out-of-plane polarized wave mode, thus the masses move only in the out-of-plane direction. All the nearest neighboring sites are linked by a linear spring with stiffness K_t while the stiffness for all the resonators is k. The first BZ of the mass-spring lattice is depicted in Fig. 2(b).

Here we define $\alpha = k/K_t$, $\beta_1 = m_r/M$, $\beta_2 = m_s/M$, and $\omega_s = \sqrt{K_t/M}$. The band structure for $\alpha = 0.6$ and $\beta_1 = \beta_2 = 1.0$ is shown as the dotted lines in Fig. 2(c) in terms of the dimensionless parameter $\Omega = \omega/\omega_s$. It can be seen that there are two Dirac cones at K point. The one located at higher frequency is consistent with the Dirac cone in a traditional hexagonal phononic lattice without resonators (the red solid lines). The other Dirac cone located right below the local resonant band gap, is the interesting one in the following study. The Eigen frequencies at the BZ corners (K and K'

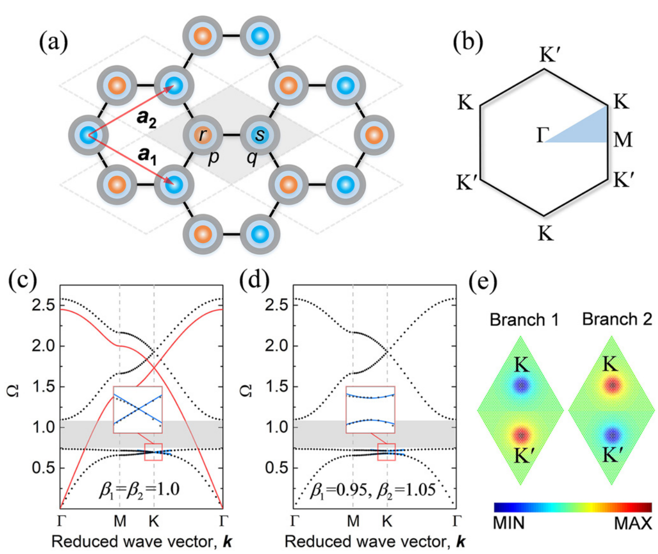

FIG. 2. Theoretical analysis based on discrete hexagonal lattice. (a) Discrete hexagonal mass-spring lattice with local resonators. (b) The first Brillouin zone (BZ). (c) The dispersion diagram for the case where the two resonators are the same (dotted lines) and that for the traditional hexagonal phononic lattice without resonators (red solid lines). (d) The dispersion diagram for the case where the masses of the two resonators are slightly different from each other. (e) The Berry curvatures for the first and second branches shown in (d).

points) are derived analytically:

$$\omega_1^2 = \frac{(\alpha+(3+\alpha)\beta_1) - \sqrt{-12\alpha\beta_1 + (\alpha+(3+\alpha)\beta_1)^2}}{2\beta_1}\omega_s^2,$$
$$\omega_2^2 = \frac{(\alpha+(3+\alpha)\beta_2) - \sqrt{-12\alpha\beta_2 + (\alpha+(3+\alpha)\beta_2)^2}}{2\beta_2}\omega_s^2,$$
$$\omega_3^2 = \frac{(\alpha+(3+\alpha)\beta_1) + \sqrt{-12\alpha\beta_1 + (\alpha+(3+\alpha)\beta_1)^2}}{2\beta_1}\omega_s^2,$$
$$\omega_4^2 = \frac{(\alpha+(3+\alpha)\beta_2) + \sqrt{-12\alpha\beta_2 + (\alpha+(3+\alpha)\beta_2)^2}}{2\beta_2}\omega_s^2. \quad (1)$$

When $\beta_1 = \beta_2 = \beta$ ($\beta = (m_r + m_s)/2/M$), two pairs of degenerated frequencies, i.e., $\omega_1 = \omega_2$ and $\omega_3 = \omega_4$ can be observed, which are directly associated with the two Dirac cones in Fig. 2(c). It is easy to prove that $\omega_1 = \omega_2 = \omega_0 < \sqrt{k/m_0}$ (where $m_0 = (m_r + m_s)/2$), indicating that the first Dirac cone must be located below the nature frequency of the local resonator. Therefore, we can control the position of this Dirac cone as needed by only tuning the local resonator. When the masses (m_r and m_s) of the resonator pair are slightly different from each other, namely, $0 < |\beta_1 - \beta_2| \ll \beta$, the degeneracy is lifted to form a band gap [Fig. 2(d)]. Next, the $k \cdot p$ perturbation method [8] will be employed to illustrate the existence of valley Hall edge state in the newly formed band gap.

The eigenstate around the valleys can be approximated by a linear combination of the degenerated eigenstates. According to the method introduced in Ref. [17], the effective model for our proposed lattice is expressed as

$$\Delta\mathbf{H}\psi = \Delta\omega\psi,$$
$$\Delta\mathbf{H} = m\sigma_z + v(\tau\Delta k_y\sigma_x - \Delta k_x\sigma_y),$$
$$m = \frac{\beta_1 - \beta_2}{B}\omega_0,\ v = \frac{\sqrt{3}S^2}{B\alpha^2}\omega_0, \quad (2)$$

where $B = 4\beta + 4[1 - (\omega_0^2\beta)/(\omega_s^2\alpha)]^2$ and $S = \beta\omega_0/\omega_s - \alpha\omega_s/\omega_0$; $\tau = -1(+1)$ denotes the $K(K')$ valley; σ_x, σ_y, and σ_z are the Pauli matrices; $\Delta\mathbf{H}$ is the effective Hamiltonian; and ψ is the eigenvector composed of the coefficients for linear combination. The blue lines in Figs. 2(c) and 2(d) are the local dispersion curves obtained by the effective model, which show good agreements with the theoretical results. To demonstrate the existence of valley Hall edge state in the band gap formed from lifting the Dirac degeneracy, we calculate the valley Chern number which is the integral of the Berry curvature over half the BZ [19]. According to the eigenvector obtained in Eq. (2), the Berry curvatures for the first and second branches can be obtained [Fig. 2(e)]. The resulting valley Chern number of the first branch is $-1/2$ $(+1/2)$ at $K(K')$ valley while that of the second branch is $+1/2$ $(-1/2)$ at $K(K')$ valley. The difference $\Delta C_v^{(K,K')} = C_{v,\mathrm{upper}}^{(K,K')} - C_{v,\mathrm{lower}}^{(K,K')} = \pm 1$ suggests the existence of valley Hall edge states in the band gap.

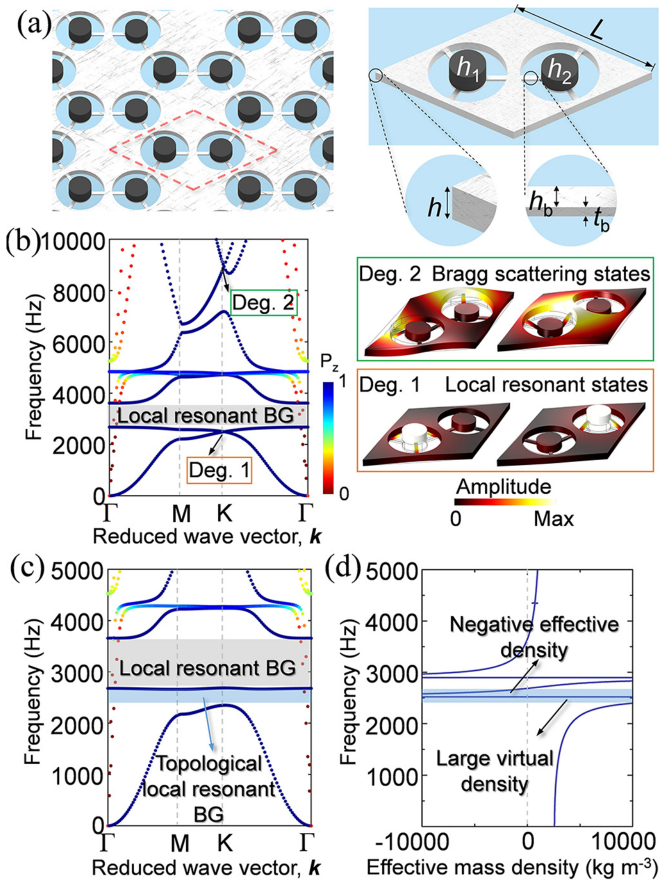

FIG. 3. (a) The designed continuous hexagonal elastic lattice. (b) The dispersion structure for the case the two resonators are the same. (c) The dispersion structure for the case the two resonators are slightly different from each other. (d) The out-of-plane effective mass density.

B. Numerical studies on the topological valley modes in continuous hexagonal lattice with local resonators

On the basis of the discrete model, a continuous hexagonal elastic lattice is designed [Fig. 3(a)]. Each unit cell has two sites, where the Aluminum ($E_{al} = 70$ GPa, $\rho_{al} = 2700\,\mathrm{kg/m^3}$ and $\upsilon_{al} = 0.33$) substrate is hollowed to form a resonator consisting of three thin beams separating each with an angle of 120 degrees and a lead ($E_l = 17$ GPa, $\rho_l = 11300\,\mathrm{kg/m^3}$, and $\upsilon_l = 0.33$) cylinder. The lattice constant is $L = 3$ cm; the thickness of the substrate plate is $h = 2$ mm; the thickness and width of the thin beams are $t_b = 0.5$ mm and $h_b = 1$ mm, respectively; the radius of the hole is $R = 7.5$ mm and that of the lead cylinder is $r = 3.5$ mm. The heights of the two lead cylinders in each unit cell are denoted as h_1 and h_2, respectively.

The band structure for $h_1 = h_2 = 2.0$ mm is shown in Fig. 3(b), where the color scale represents the degree of polarization. Here, we focus on the out-of-plane polarized mode, i.e., the branches in blue color. In the observed frequency range, two Dirac degeneracies appear at K point. The Dirac degeneracy located at relatively high frequency is the classical one in the substrate hexagonal lattice with circular holes. We can see that although Dirac degeneracy at K point

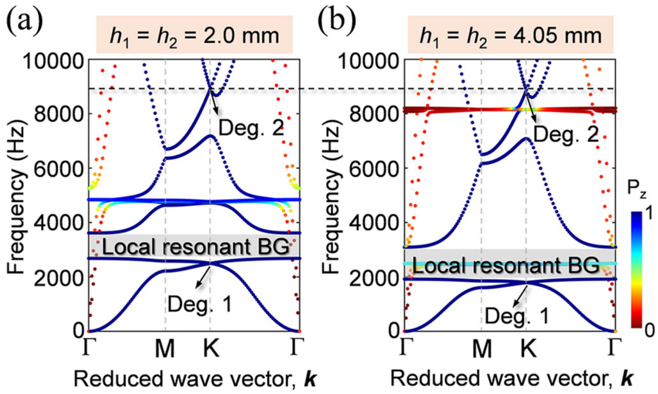

FIG. 4. The dispersion curves for (a) $h_1 = h_2 = 2.0$ mm and (b) $h_1 = h_2 = 4.05$ mm.

definitely appears in the substrate hexagonal lattice possessing C_{6v} symmetry; however, no full band gap appears in this case when the degeneracy is lifted by breaking inversion symmetry. In comparison, the other Dirac degeneracy located right below the resonant frequency can avoid this problem. This Dirac degeneracy is produced by the double local resonant effect on the basis that the substrate lattice satisfies C_{6v} symmetry, see the inserted mode shapes [Fig. 3(b)]. Its frequency is mainly determined by the nature frequency of the resonators. Therefore, we can easily tune Dirac frequency by changing the natural frequency of the resonators without altering the lattice constant. As demonstrated in Fig. 4, when the resonant frequency of the resonators is altered through increasing the height of the lead cylinders, the local resonant Dirac cone shifts correspondingly, meanwhile the Bragg scattering Dirac cone almost remains unchanged since the lattice constant has not been modified. In addition to single Dirac cone, fourfold degenerated double Dirac cone induced by local resonant states can also be achieved by employing band folding technique [35]; see Appendix A for details.

When the resonant frequencies of the two resonators are slightly different from each other, the frequencies corresponding to the local resonant states shown in Fig. 3(b) become different. Therefore, the Dirac degeneracy is lifted, giving rise to a complete band gap corresponding to the out-of-plane polarized mode. This mechanism is illustrated in Fig. 3(c), which shows the band structure for the case $h_1 = 2.3$ mm and $h_2 = 1.7$ mm. In addition, we calculate the out-of-plane effective mass density for this case [Fig. 3(d)]. The two straight lines correspond to the natural frequencies of the two resonators, respectively. The frequency range corresponding to the band gap formed from lifting Dirac degeneracy is highlighted in blue. It's found that this band gap is related to the local resonance of the resonator, which results in mixing effective negative mass effect and Bragg scattering effect due to large virtual mass.

Next, to demonstrate the existence of interface edge modes in the topological local resonant band gap, the band diagram of a strip supercell [Fig. 5(a)] with an interface composed of 8 unit cells with different topological valley phase at either side is illustrated in Fig. 5(b). Here we only focus on the blue branches corresponding to the out-of-plane polarized modes.

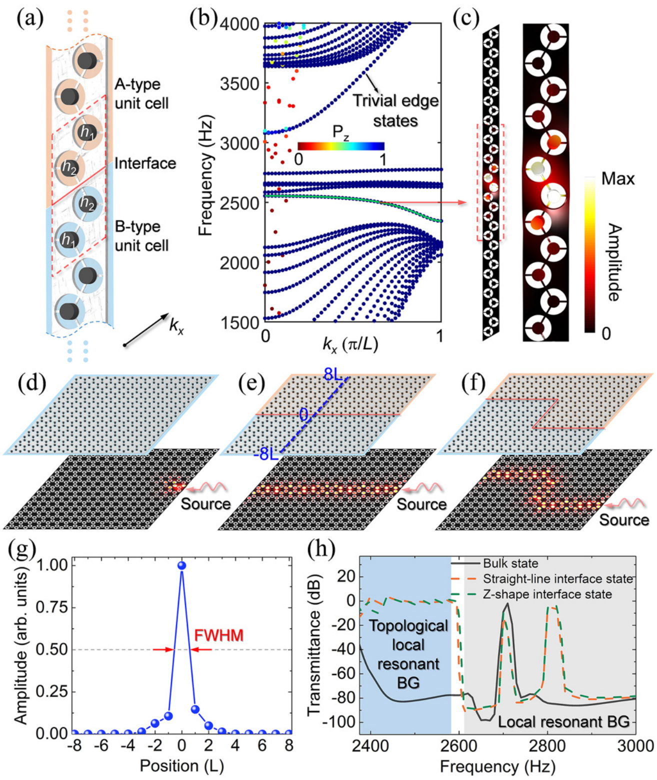

FIG. 5. Numerical analysis of the local resonant topological interface state. (a) The FE model of the strip supercell. (b) Band structure of the strip, where the green solid line represents the interface branch. (c) Eigenvector corresponding to the interface mode evaluated at $f = 2500$ Hz. (d–f) The displacement fields at $f = 2500$ Hz for the bulk state, straight-line interface state and Z-shape interface state, respectively. (g) Simulated displacement amplitude profile of a cutline shown in (e), where position "0" corresponds to the resonators closest to the interface. (h) Calculated transmission spectra of the three states under study.

Among these modes, an interface mode is observed shown in green solid line. For instance, one eigenvector corresponding to the interface mode is illustrated in Fig. 5(c), where the displacement field localizes at the interface and decays rapidly away from it. Moreover, the interface mode shows strong localized vibration on the resonator while the substrate is almost at rest.

To further characterize the propagation behavior of the topological valley edge modes, full-field frequency domain simulations with low-reflecting boundary condition are conducted. An out-of-plane harmonic excitation at 2500 Hz, which is located in the topological band gap, is applied at the position shown with red wavy arrow. Figure 5(d) shows the displacement field for the bulk state, which indicates that the bulk lattice plate is insulating due to the presence of band gap therein. In comparison, for both the straight-line [Fig. 5(e)] and Z-shape [Fig. 5(f)] interface configurations, the induced flexural waves propagate along the interface. Figure 5(g) illustrates the displacement amplitude profile of a cutline shown in Fig. 5(e). The full width at half maximum (FWHM) of the peak in Fig. 5(g) is about 1.16L, where L is the lattice constant. This indicates that vibrations strongly

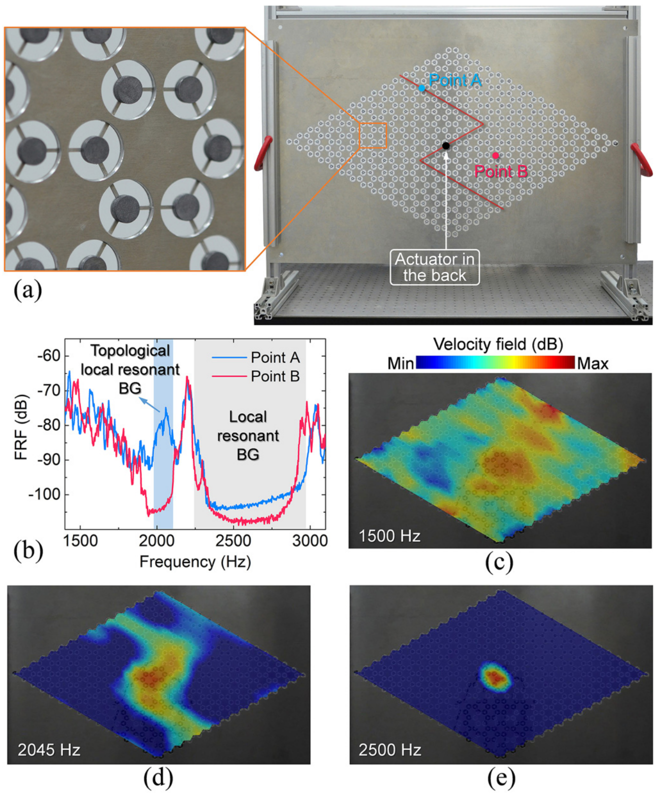

FIG. 6. Experimental demonstration of the local resonant topological interface state. (a) The fabricated lattice sample and the experimental setup. (b) The measured frequency-response functions (FRF) of the displacements at points A and B. (c–e) The measured root mean squared distributions of the velocity field at 1500, 2045, and 2500 Hz, respectively.

localize at the interface. Besides, the transmission spectra for the above three lattice structures are calculated [Fig. 5(h)]. Over the frequency range supporting topological protected edge states (blue shaded area), wave propagations along both the straight-line interface and the Z-shape interface have high transmission as compared to the bulk state. Quantitatively, the average amplitude ratio between the output and input displacements over 2430–2560 Hz for the Z-shape interface path is 96%, while that for the straight-line interface path is 99%. This indicates that the valley interface state introduced by the local resonance is marginally affected by the bends. In comparison, for frequencies located in the trivial local resonant band gap (grey shaded area), all those three structures have very low transmission except for several peaks.

C. Experimental observation of topologically protected interface waves

Furthermore, a lattice sample with the same microstructure parameters as the numerical model is fabricated, together with the experimental setup shown in Fig. 6(a). Out-of-plane excitation is applied at the position shown with black point. A Z-shaped interface path is highlighted with the red line. Figure 6(b) shows the measured frequency-response functions (FRF) of the displacements at points A (lies on the interface path) and B (located in the bulk). Two low transmittance areas are marked with the blue and grey rectangles, respectively. In the grey area, low transmittances are observed for both points A and B. However, a transmission enhancement of approximately 20 dB for point A as compared to point B is found in the blue area, which demonstrates the existence of interface propagating state. Therefore, the blue low transmittance area is related to the topological local resonant BG while the grey low transmittance area is related to the trivial one of the designed lattice. To verify it, the experimental root mean squared distributions of the velocity field at 2045 Hz, which is located in the topological local resonant BG, is shown in Fig. 6(d). The induced out-of-plane wave travels along the interface and decays rapidly in the direction perpendicular to the interface. In contrast, for frequency located in the trivial local resonant BG, the excited wave is prohibited to propagate in the whole plate [Fig. 6(e)]. For reference, the measured velocity field for the frequency located in the pass band is shown in Fig. 6(c). It should be noted that the resonators and the substrate are fabricated separately, and then bonded together with glue. Therefore, the stiffness of the microstructure is reduced, resulting in the decrease of frequency of the BGs as compared to the numerical results. When using the real parameters retrieved from the experimental results, the calculations coincide with the experiments (see the Appendix B for details). In addition, the measured wave field shows visible decay along the interface [Fig. 6(d)], this is mainly due to the damping effect introduced by the glue used to bond the microstructure beams (see the Appendix C for details).

III. CONCLUSIONS

In summary, we report Dirac degeneracies induced by the local resonant states, whose frequency is determined by the nature frequency of resonators rather than the lattice constant. After gapping the Dirac cone, topological edge modes exist in the newly formed local resonant band gap, as observed by both numerical simulations and experimental measurements. Our study provides an effective approach of producing robust elastic topological interface states over desired frequency ranges and demonstrates the propagation behavior of the topological interface modes in local resonant band gap.

ACKNOWLEDGEMENTS

This work was supported by the National Natural Science Foundation of China (Grants No. 11632003, No. 11972083, No. 11802017, No. 11991030, No. 11991031, and No. 11991033) and the Postdoctoral Innovation Talents Support Program (Grant No. BX20180040).

APPENDIX A: FOURFOLD DEGENERATED DOUBLE DIRAC CONE INDUCED BY LOCAL RESONANT STATES

In addition to single Dirac cone, fourfold degenerated double Dirac cone located at any desired frequency can also be achieved by employing band folding method. To realize band folding, an enlarged unit cell (supercell) is chosen, as shown in Fig. 7(a). The first BZs corresponding to the original unit cell and the supercell are plotted in Fig. 7(b) for comparison,

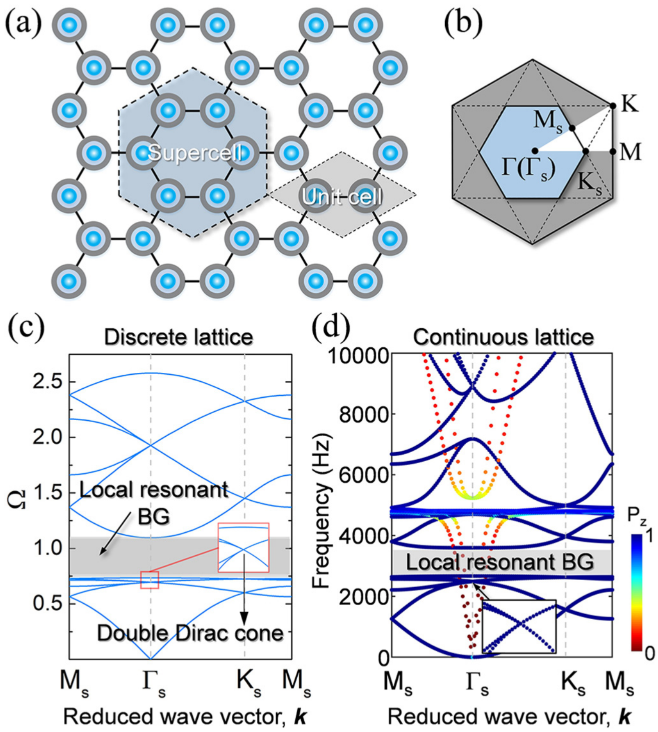

FIG. 7. Realization of double Dirac cone at desired frequency based on local resonant effect. (a) Schematic of the lattice with local resonators. (b) The first BZs of the original unit cell and the supercell. The calculated dispersion diagrams for (c) discrete lattice model and (d) solid continuous lattice model.

which indicates that the first BZ of the supercell is obtained through folding that of the original unit cell along the dotted lines. Correspondingly, the band structure of the supercell can be obtained by folding the band structure shown in Fig. 2(c), which is the band structure of the original unit cell. The detailed band folding mechanism can be seen in Ref. [35]. Figure 7(c) represents the resulting dispersion relation of the supercell. Two double Dirac cones can be observed at Γ_s ($\mathbf{k} = 0$). The one located at relatively low frequency is right below the local resonant band gap induced by the resonators. This means that we can produce double Dirac cone and corresponding spin Hall edge states at any desired frequency by controlling the nature frequency of the embedded resonators. The dispersion analysis based on the solid continuous lattice model [as depicted in Fig. 3(a)] also confirms this conclusion, as shown in Fig. 7(d).

APPENDIX B: CALCULATIONS USING THE REAL PARAMETERS RETRIEVED FROM THE EXPERIMENTAL RESULTS

In the experiments, the resonators and the substrate are fabricated separately and then bonded together with glue. Therefore, the stiffness of the microstructure is reduced, resulting in the decrease of frequency of the BGs as compared to the numerical results. To verify this assertion, we retrieve the real stiffness of the microstructure beam from the experimental results and calculate the band structure of the strip supercell again. In the simulation, the thickness of the thin

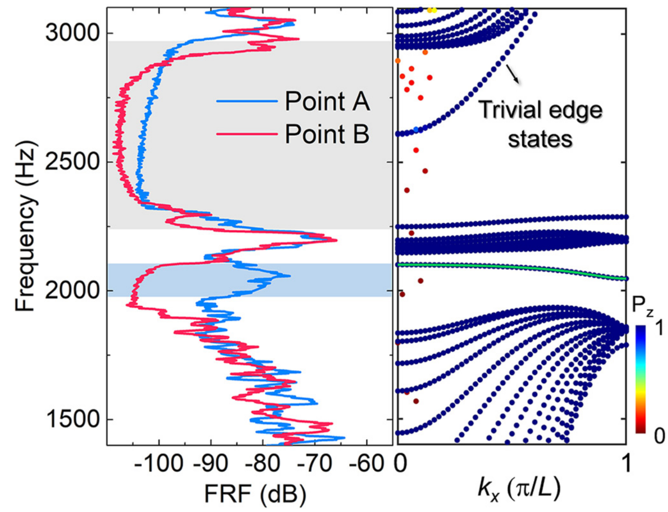

FIG. 8. (left) The measured frequency-response functions. (right) Band structure of the strip supercell calculated by using the real stiffness of the microstructure beam retrieved from the experimental results. Good agreements between the calculations and experiments are observed.

beams is retrieved to be $t_b = 0.42$ mm. As shown in Fig. 8, good agreements between the calculations and experiments are observed. In this case, space-inversion symmetry (SIS) breaking is strong, since the stiffness of the resonators is reduced while the mass difference between the two resonators remains the same. As a result, the bandwidth of the valley interface state (the green line in Fig. 8) becomes smaller.

APPENDIX C: CALCULATED DISPLACEMENT FIELDS WITH THE EFFECT OF MATERIAL DAMPING

To demonstrate that the decay along the interface route is due to the material damping, we calculate the displacement fields with the effect of material damping of the local resonators, as shown in Fig. 9. Obvious decay along the interface route can be observed when the damping coefficient of the microstructure beam is assumed to be 1%.

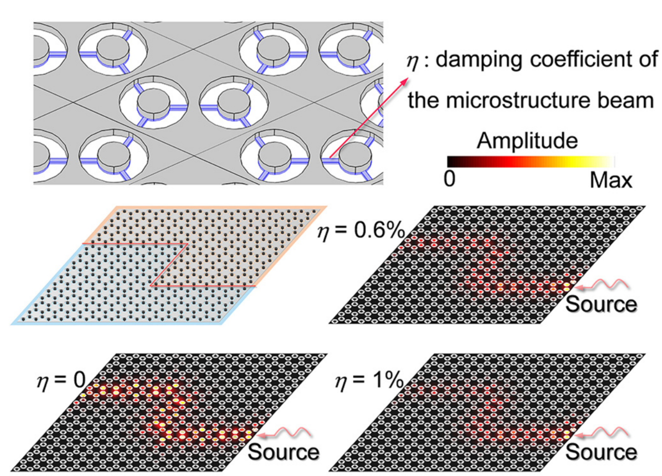

FIG. 9. The calculated displacement fields with effect of material damping for Z-shape interface route at $f = 2500$ Hz.

[1] M. Z. Hasan and C. L. Kane, Rev. Mod. Phys. **82**, 3045 (2010).
[2] F. D. M. Haldane and S. Raghu, Phys. Rev. Lett. **100**, 013904 (2008).
[3] Z. Wang, Y. D. Chong, J. D. Joannopoulos, and M. Soljacic, Phys. Rev. Lett. **100**, 013905 (2008).
[4] Z. Wang, Y. Chong, J. D. Joannopoulos, and M. Soljacic, Nature **461**, 772 (2009).
[5] Z. Yang, F. Gao, X. Shi, X. Lin, Z. Gao, Y. Chong, and B. Zhang, Phys. Rev. Lett. **114**, 114301 (2015).
[6] R. Fleury, A. B. Khanikaev, and A. Alu, Nat. Commun. **7**, 11744 (2016).
[7] C. He, X. Ni, H. Ge, X. C. Sun, Y. B. Chen, M. H. Lu, X. P. Liu, and Y. F. Chen, Nat. Phys. **12**, 1124 (2016).
[8] J. Lu, C. Qiu, L. Ye, X. Fan, M. Ke, F. Zhang, and Z. Liu, Nat. Phys. **13**, 369 (2016).
[9] C. L. Kane and T. C. Lubensky, Nat. Phys. **10**, 39 (2013).
[10] J. Paulose, A. S. Meeussen, and V. Vitelli, Proc. Natl. Acad. Sci. U.S.A. **112**, 7639 (2015).
[11] L. M. Nash, D. Kleckner, A. Read, V. Vitelli, A. M. Turner, and W. T. Irvine, Proc. Natl. Acad. Sci. U.S.A. **112**, 14495 (2015).
[12] P. Wang, L. Lu, and K. Bertoldi, Phys. Rev. Lett. **115**, 104302 (2015).
[13] S. H. Mousavi, A. B. Khanikaev, and Z. Wang, Nat. Commun. **6**, 8682 (2015).
[14] S. Y. Yu, C. He, Z. Wang, F. K. Liu, X. C. Sun, Z. Li, H. Z. Lu, M. H. Lu, X. P. Liu, and Y. F. Chen, Nat. Commun. **9**, 3072 (2018).
[15] M. Miniaci, R. K. Pal, B. Morvan, and M. Ruzzene, Phys. Rev. X **8**, 031074 (2018).
[16] J. Cha, K. W. Kim, and C. Daraio, Nature **564**, 229 (2018).
[17] Y. Chen, X. Liu, and G. Hu, J. Mech. Phys. Solids **122**, 54 (2019).
[18] H. Chen, H. Nassar, A. N. Norris, G. K. Hu, and G. L. Huang, Phys. Rev. B **98**, 094302 (2018).
[19] J. Vila, R. K. Pal, and M. Ruzzene, Phys. Rev. B **96**, 134307 (2017).
[20] M. Yan, J. Lu, F. Li, W. Deng, X. Huang, J. Ma, and Z. Liu, Nat. Mater. **17**, 993 (2018).
[21] H. Zhu, T. W. Liu, and F. Semperlotti, Phys. Rev. B **97**, 174301 (2018).
[22] T. W. Liu and F. Semperlotti, Phys. Rev. Appl. **11**, 014040 (2019).
[23] Q. Zhang, Y. Chen, K. Zhang, and G. Hu, Extreme Mech. Lett. **28**, 76 (2019).
[24] M. Miniaci, R. K. Pal, R. Manna, and M. Ruzzene, Phys. Rev. B **100**, 024304 (2019).
[25] S. Yves, R. Fleury, T. Berthelot, M. Fink, F. Lemoult, and G. Lerosey, Nat. Commun. **8**, 16023 (2017).
[26] S. Yves, R. Fleury, F. Lemoult, M. Fink, and G. Lerosey, New J. Phys. **19**, 075003 (2017).
[27] D. Zhao, M. Xiao, C. W. Ling, C. T. Chan, and K. H. Fung, Phys. Rev. B **98**, 014110 (2018).
[28] Z. Zhang, Y. Cheng, X. Liu, and J. Christensen, Phys. Rev. B **99**, 224104 (2019).
[29] Z. Zhang, Y. Gu, H. Long, Y. Cheng, X. Liu, and J. Christensen, Research **2019**, 5385763 (2019).
[30] R. Chaunsali, C.-W. Chen, and J. Yang, Phys. Rev. B **97**, 054307 (2018).
[31] D. Torrent, D. Mayou, and J. Sánchez-Dehesa, Phys. Rev. B **87**, 115143 (2013).
[32] R. K. Pal and M. Ruzzene, New J. Phys. **19**, 025001 (2017).
[33] R. Chaunsali, C.-W. Chen, and J. Yang, New J. Phys. **20**, 113036 (2018).
[34] W. Wang, B. Bonello, B. Djafari-Rouhani, and Y. Pennec, Phys. Rev. B **100**, 140101(R) (2019).
[35] L. H. Wu and X. Hu, Phys. Rev. Lett. **114**, 223901 (2015).